修　士　論　文

Photometric Stereo with Auto-Radiometric Calibration

(カメラ応答関数の自動校正を伴う照度差ステレオ)

東京大学大学院
情報理工学系研究科
電子情報学専攻

48-116443　モンコンマーン　ウィーンナート

指導教員　　佐藤 洋一　教授

Abstract

This thesis presents photometric stereo with auto-radiometric calibration to estimate surface orientations from a sequence of object images taken under different lighting directions with a radiometrically uncalibrated camera. The original photometric stereo assumes the images are captured by a camera with a linear response function. However, cameras often have a non-linear response function, and thus, the radiometric calibration is required to cancel the effect of nonlinear response function before taking images which are later used for physics-based analysis of the scene. Unfortunately, the radiometric calibration is a time-consuming pre-process requiring many additional images.

The goal of this study is to achieve photometric stereo with auto-radiometric calibration that can estimate surface orientations from radiometrically uncalibrated images with no additional image required. With this method, one can apply photometric stereo with images taken by a camera whose response function is unknown.

The key idea behind this work is to make use of the consistency between the irradiance converted from the inverse response function and the irradiance estimated from a reflection model, more specifically, Lambertian model in this work. Consequently, a linear optimization problem can be formulated to estimate the surface normals of a Lambertian surface and the response function simultaneously. To handle non-Lambertian surfaces, the proposed method is further extended for discarding specular highlights with a RANSAC-like approach where surface orientations and a camera response function can be estimated simultaneously in the face of specular highlights.

Experiments were conducted using both synthetic objects and real objects, demonstrating the effectiveness of the proposed method successfully.

Acknowledgements

First of all, I would like to express my gratitude to my advisor, Professor Yoichi Sato. Not only for his guidance and advices but also his kindness support to let me have wonderful experience while I am in Japan. I also would like to thank Takahiro Okabe for his insightful advices and his encouragement. I have learned a lot from him about thinking in the scientific way.

I would like to thank all wonderful members in Sato-lab for their friendship. I was fortunate to have a chance to know and work with these geniuses. I also would like to thank the secretaries, Sakie Suzuki, Yoko Imagawa and Chio Usui for their kindness. They helped me from the start even before I come to Japan regarding visa documents, application, and various procedures. My gratitude also goes to my Thai friends who make me feel like I am at home while I am in Japan, and help me get through many problems.

I am grateful to Panasonic Scholarships who gives me the opportunity and financial aids during my Master course in Japan. Moreover, the Scholarships' staffs always take a good care of me and always ask if I need any assistance or having any problems regarding living and studying in Japan.

Finally, my deepest gratitude goes to my family: my parents, my sister, as well as my late grandmother for their support. I could never have completed this thesis without them.

Contents

List of Figures **v**

List of Tables **vi**

1 Introduction **1**

2 Related Work **3**
2.1 Radiometric Calibration 3
2.2 Photometric Stereo for Non-Lambertian Surfaces 5
2.3 Relation to the Previous Works 7

3 Photometric Stereo with Auto-Radiometric Calibration **8**
3.1 Background 8
3.2 Proposed Method 8
3.2.1 Lambertian Reflection Model 8
3.2.2 Photometric Stereo 9
3.2.3 Radiometric Response Function 10
3.2.4 The Simultaneous Estimation 11
3.3 Experiments 12
3.3.1 Synthetic Images 12
3.3.2 Real Images 16

4 Extension for Non-Lambertian Materials **20**
4.1 Background 20
4.2 Proposed Method 22
4.3 Experiments 24
4.3.1 Synthetic Images 25
4.3.2 Real Images 28

5 Conclusions **38**

Bibliography **40**

Publications **43**

List of Figures

1.1 Photometric stereo with auto-radiometric calibration using irradiance consistency 2

2.1 Radiometric calibration using multiple images with varying exposures. 4
2.2 The surface normals recovered from four triplets of light sources . . 6

3.1 Lambertian reflection and specular reflection 9
3.2 Synthetic images of sphere and face with different radiometric response functions. 13
3.3 Results using synthetic images 14
3.4 Results using synthetic images: face. 15
3.5 Real images of sphere and statue with different radiometric response functions. 17
3.6 Results using real images: sphere. 18
3.7 Results using real images: statue. 19

4.1 Overview of the extension for non-Lambertian surfaces. 21
4.2 Response functions used in the experiments 25
4.3 Synthetic images: Sphere 26
4.4 The estimated normal map of the synthetic images: sphere (agfapan) 27
4.5 The estimated normal maps of the synthetic images: sphere (agfascala). 27
4.6 The estimated inverse response functions. 28
4.7 Real images: (a) SEAL (b) GHOST (c) TOMATO (d) FISH 29
4.8 The estimated normal maps of the real images: SEAL (agfascala). . 31
4.9 The estimated normal maps of the real images: SEAL (agfapan). . . 32
4.10 The estimated normal maps of the real images: GHOST (agfascala). 33
4.11 The estimated normal maps of the real images: GHOST (agfapan). 34
4.12 The estimated normal maps of the real images: TOMATO (agfapan). 34

4.13 The estimated normal maps of the real images: TOMATO (agfascala). 35
4.14 The estimated normal maps of the real images: FISH (agfapan). . 35
4.15 The estimated normal maps of the real images: FISH (agfascala). . 36
4.16 The estimated response functions for SEAL, GHOST, TOMATO and FISH. 37

5.1 The generalized bas-relief ambiguity 39

List of Tables

3.1 Average errors of estimated surface normals and RMS errors of estimated inverse radiometric response functions: synthetic images. . 13
3.2 Average errors of estimated surface normals and RMS errors of estimated inverse radiometric response functions: real images. 17

4.1 The estimation results for the synthetic sphere. 26
4.2 The estimation results for the real images sphere 30

Chapter 1

Introduction

Scene reconstruction is one of the fundamental problems in computer vision. Many methods have been proposed to recover the geometry of a scene, such as time-of-flight cameras, laser range scanners and multi-view stereo. Photometric stereo is a technique for recovering surface orientations from multiple images of a stationery object taken under different lightings. Its advantage over the other shape reconstruction methods is the ability to recover surface orientations accurately using an ordinary camera.

The basic photometric stereo assumes that a static object follows the Lambertian reflection model and that the directions and intensities of directional light sources are known a priori. These assumptions limit photometric stereo from being carried out in uncontrolled environments. Therefore, the research trend in photometric stereo can be seen in two directions: the generalization of materials and the generalization of light sources.

This thesis addresses another common assumption in many computer vision algorithms, including photometric stereo, that is image intensity is proportional to the radiance of the corresponding light falling onto a camera sensor, *e.g.*, images are captured by a camera with linear response. Unfortunately, ordinary cameras often have nonlinear response functions, and such cameras are indeed intentionally designed to have non-linear response in order to compress dynamic range of scenes, to simulate the characteristic of film imaging systems or to compensate for the nonlinearity of display systems. Although it benefits to display systems, this nonlinearity may lead to unsatisfactory corrupted results in many computer vision methods which assume a linear camera response function. Thus, a calibration of radiometric response of a camera is required to cancel the effect of the non-linearity before being used for photometric analysis.

Most of the radiometric calibration techniques make use of an image sequence of a static scene taken under varying exposure times. The ratio between the exposure times and the observed image intensities are used to estimate a response function.

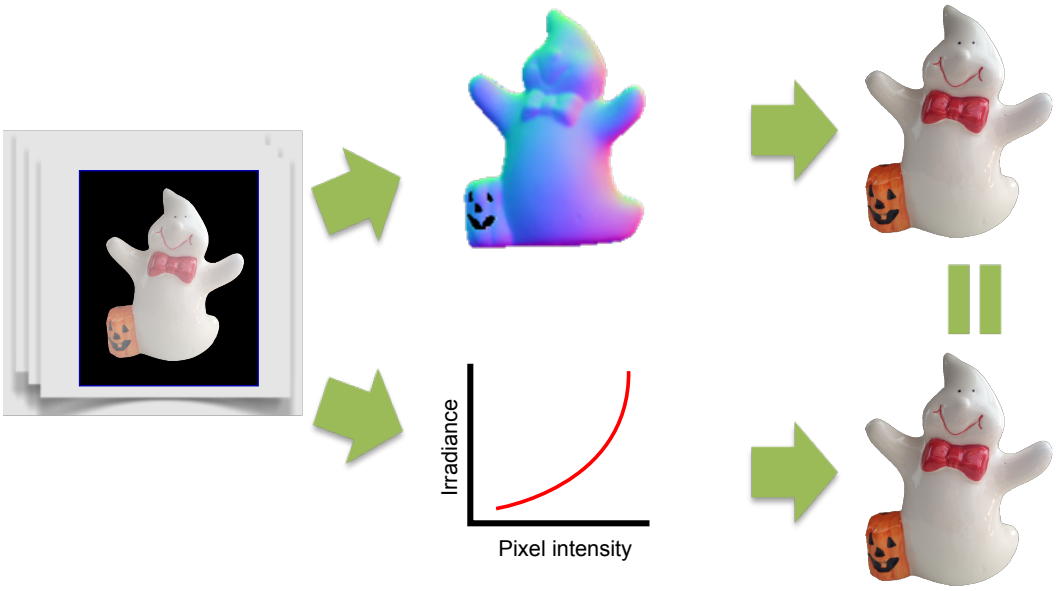

Figure 1.1: Photometric stereo with auto-radiometric calibration using irradiance consistency. The irradiance estimated from surface property (top) must equal to the irradiance estimated from the inverse response function (bottom).

Because these methods require a number of additional images, they are often time-consuming and cumbersome.

We present a novel method that avoids radiometric calibration preprocessing from photometric stereo. Our proposed method simultaneously estimates the surface normals of the target object and an inverse radiometric response function, which maps a pixel value to an image irradiance value. The key idea of our method is to make use of the consistency between the inverse radiometric response functions and the surface normals; the irradiance values converted from the inverse radiometric response function should equal to the corresponding irradiance values calculated from the surface normals (figure 1.1). In other words, we take advantage of such a clue, which is inherent in the physical model of reflectance itself, to estimate surface normals as well as inverse radiometric response functions.

The remainder of this thesis is organized as follows: Chapter 2 introduces some related works in the radiometric calibration and the photometric stereo. In Chapter 3, we describe the photometric stereo with auto-radiometric calibration by using irradiance consistency and the experimental results. We present the extension for non-Lambertian materials in Chapter 4, and concluding remarks in Chapter 5.

Chapter 2

Related Work

This chapter explains some related work in the photometric stereo and the radiometric calibration. The relationship of our proposed method to the previous works is also described.

2.1 Radiometric Calibration

Radiometric calibration is a process to estimate a response function of a camera in order to subsume irradiance values from image intensities. The most widely used approach assumes scene radiance remains unchanged along an image sequence. Hence, sensor irradiance becomes proportional to exposure times so that it allows the estimation of the response function without prior information regarding the scene radiance.

The pioneering work on the linearity of response function can be seen in the work proposed by Mann and Picard [19]. They proposed a method that uses two images of a static scene taken under different known exposures to compute a parametric response function in a form of gamma curve. Given the ratio of the exposure between the first and the second image R, an unknown measurement I at a pixel p_0 of the first image leads to the measurement RI at the pixel p_0 of the second image. Then, the pixel p_1 with the measurement RI at the first image is sought and leads the measurement R^2I in the second image at the pixel p_1. The search continues to obtain the series of measurement $I_0, RI_0, R^2I, R^3I, \ldots$. Regression is applied to find the parameters for the response function. Devebec and Malik[5] use a smoothness constraint to estimate a non-parametric response function. In contrast to [19], this method uses the entire images instead of some parts of the images, and achieves better accuracy. However, it needs precisely measured exposure ratios.

One of the most widely used methods is the work by Mitsunaga and Nayar [20].

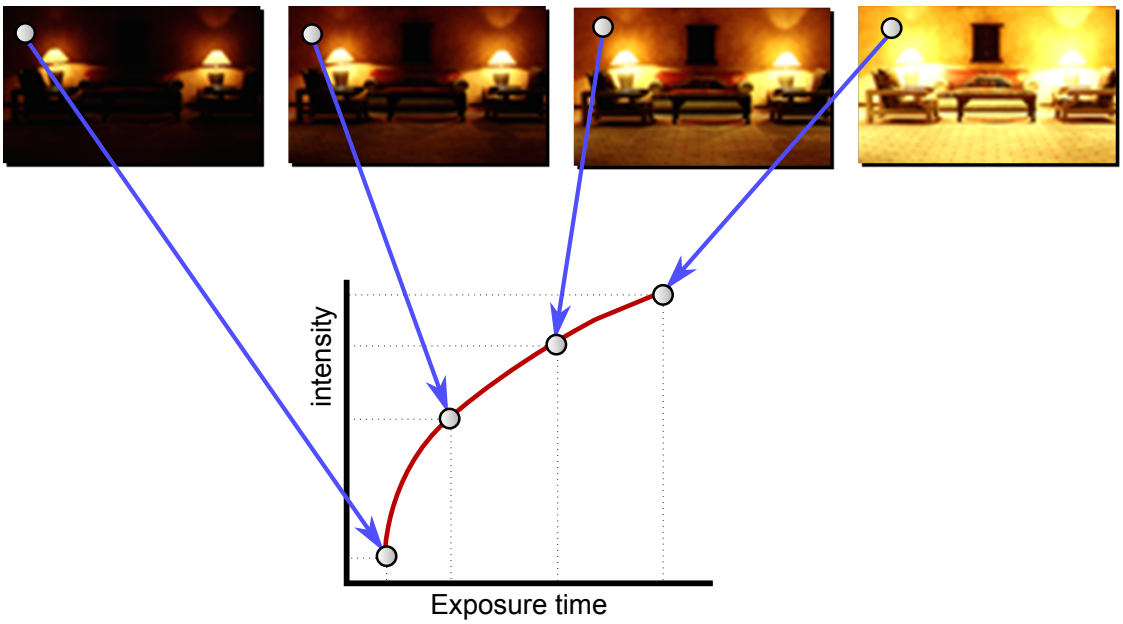

Figure 2.1: Radiometric calibration using multiple images with varying exposures.[20]

They use a rough estimation of exposure ratios to approximate a response function with polynomials. However, these methods are limited in that they require many additional images for radiometric calibration.

Lin *et al.* [17] avoid using multiple images by using color mixtures of edge areas between two regions to perform radiometric calibration. Under the effect of a nonlinear response function, the image irradiances at the edge area are no longer linear combinations of the image irradiance of those regions. Therefore, the function that recovers the linearity of the color mixtures is the nonlinear response function. The method proposed in [18] uses similar approach to determine the response function from a single grayscale image.

There are some methods that allow movement of the camera. Wilburn *et al.* [27] conduct radiometric calibration on the basis of motion blur in a single image. They make use of temporal irradiance mixtures instead of spatial ones. Kim and Pollefeys [15] estimate a radiometric response function from an image sequence taken with a moving camera by computing pixel correspondences across the image frames. Grossberg and Nayar [10] show that radiometric calibration can be done by using the intensity histograms of two image frames without exact registration.

The recent work by Lee *et al.* [16] formulates the radiometric calibration as a rank minimization problem. It arranges the observations, *e.g.* an image sequence

taken under different exposures, in a matrix form so that a column vector corresponds to an observation vector. This observation vector can be both the observations from multiple images taken under multiple exposures, or the color mixtures around the edge area. Because the observation vectors should be linearly dependent, the inverse response function can be estimated as an element-wise function that minimizes the rank of the observation matrix.

Shi *et al.* [25] proposed a radiometric calibration technique which uses images that taken under varying light sources *e.g.* input images for photometric stereo. They investigate a color profile, *i.e.* the set of RGB values at a certain pixel under different light sources, and demonstrate that input images to photometric stereo can be used also for radiometric calibration. Their method is based on the observation that a color profile draws a straight line (curve) in RGB space when a radiometric response function is linear (nonlinear). Therefore, they estimate a radiometric response function as a function that linearizes the color profiles.

2.2 Photometric Stereo for Non-Lambertian Surfaces

As previously mentioned, the classic photometric stereo[28] is a technique to estimate the surface normals of an object from a sequence of images captured by a fixed camera. It assumes the object is illuminated under varying light sources and, importantly, obeys the Lambertian model.

However, specular highlights observed in a wide range of real-world materials such as ceramics and plastics violate the Lambertian reflection property, and as a result, the estimated surfaces are distorted by specular highlights.

Therefore, there are a lot of photometric stereo techniques have been proposed to estimate the surface normals of such materials. The techniques for photometric stereo for non-Lambertian surfaces can be classified in two categories, modeling approach and statistical approach.

The modeling approach assumes target objects follows a specific reflection model, and then estimates parameters of the reflectance model along with the surface normals. The examples of this approach can be seen in [23, 26, 9, 8]. Nayer *et al.* [23] assume a hybrid reflectance model that is a linear combination of Lambertian and specular components. Tagare and de Figueiredo [26] consider diffuse non-Lambertian surfaces and solve the problem using an m-lobed reflectance map. Goldman *et al.* [9] assume a material can be composed of multiple fundamental materials, each described with a parametric *Bidirectional reflectance distribution function (BRDF)* model. Therefore, we can estimate the surface made of the mixture of fundamental materials if we know the reflectance parameters of each

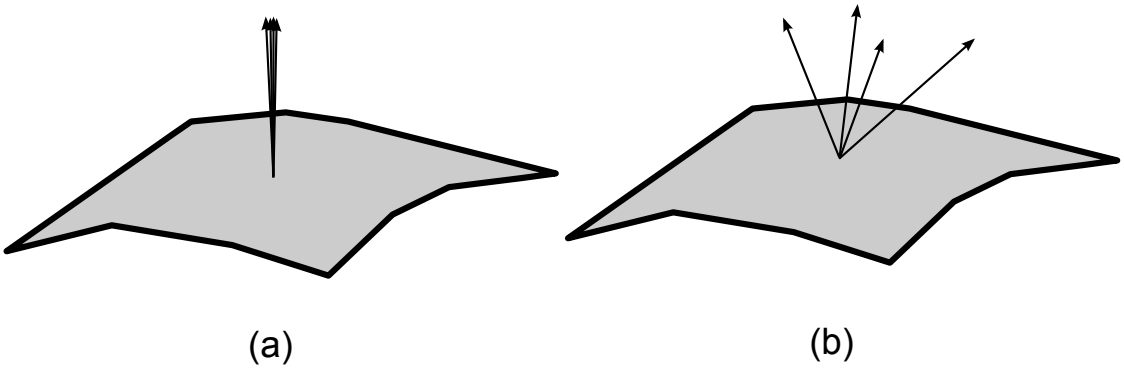

Figure 2.2: The surface normals recovered from four triplets of light sources (a) when no specularity is observed. (b) when specularity is observed.

fundamental materials. Georghiades [8] considers both diffuse and specular reflections and estimates surface normals as well as reflectance parameters based on the Torrance-Sparrow model with unknown light directions. This approach is efficient when the BRDF reflection model is precisely assumed. More importantly, it is difficult to estimate the BRDF parameters accurately with a few numbers of observations.

The statistical approach regards specular pixels, shadows as well as other corrupted measurements as outliers and excludes them from the surface estimation. For example, Coleman and Jain[14] proposed a photometric stereo technique for non-Lambertian surface using four light sources. They detect highlights by using the recovered albedos, *i.e.*, the reflectance factors. Specifically, they estimated four candidate albedos at a certain location from four possible triplets selected from four light sources. If all of the candidate albedos do not coincide, it is regarded due to specularity, and the smallest albedo is used for surface estimation. Barsky and Petrou[2] extended the method to detect highlight and shadow regions. Because four light sources are linearly dependent if they are not in the same plane, they treat highlights and shadows as outliers that violate a linear model derived from the Lambertian model and linear dependency of the light sources.

In additional to the four-source photometric stereo techniques, there are several outliers removal techniques that treat specular highlights as sparse errors. Wu *et al.* [29] casts the photometric stereo problem as a problem of completing and recovery of a low-rank matrix. Suppose only a small fractions of the pixels in each image are specular highlights and most of pixels are illuminated by the light source, we can decompose an observation matrix $\boldsymbol{O}$ into a summation of a low-rank matrix $\boldsymbol{D}$, which represent an ideal diffusive irradiance, and a sparse error matrix $\boldsymbol{E}$ which represents the deviation due to the specularity, shadows, as well as other corrupted measurements. Then, find the sparse matrix $\boldsymbol{E}$ that minimizes the rank

of $\boldsymbol{D}$. With known light source directions and intensities, the surface normals can be estimated from the low-rank matrix $\boldsymbol{D}$. Instead of using robust principle component analysis as in [29], Ikehata *et al.* [13] use a hierarchical Bayesian model derived from a sparse Bayesian learning framework.

Unfortunately, these techniques assume input images are captured by a camera with a linear response function. Therefore, we cannot directly use these techniques in our case due to nonlinearity of a response function.

2.3 Relation to the Previous Works

In this thesis, we present our photometric stereo with auto-radiometric calibration. Although we can use an existing radiometric calibration technique as a completely independent preprocess, the calibration techniques are often cumbersome and usually require additional images. Unlike the other radiometric calibration techniques, our proposed method requires no additional images used for radiometric calibration. More importantly, our method is based on a different clue; we take advantage of the physical model of reflectance for radiometric calibration.

Our technique is similar as Shi *et al.*[25] that is the input images are captured under varying illuminations by a fixed camera. However, their method is still considered as a preprocessing, requires nonlinear optimization and the input images must be color images. More importantly, their method cannot handle a certain class of radiometric response functions such as a polynomial and gray objects which the color profiles remain straight lines even the radiometric response function is nonlinear.

As for the extension to handle the non-Lambertian surfaces, we integrate a RANSAC-like robust estimation [7] to our framework to determine specular region and estimate response function by maximizing the inlier pixels to the Lambertian model. RANSAC has been used by several works to handle specular highlights in face recognition task [24] and to remove specularity from non-Lambertian surfaces in photometric stereo [12] [11]. Mukaigawa *et al* [22] use RANSAC to classify diffuse and specular region using images taken under different light sources.

As far as we know, ours is the only method that can estimate surface normals and a radiometric response function simultaneously. In addition, our method does not require nonlinear optimization and color images, and it can also handle polynomial response functions and gray objects.

Chapter 3

Photometric Stereo with Auto-Radiometric Calibration

3.1 Background

To avoid the radiometric calibration, we present a novel method to perform photometric stereo with auto-radiometric calibration. The key idea of our method is to make use of the consistency between an inverse radiometric response function and surface normals; the irradiance values converted from pixel values by using the inverse radiometric response function should be equal to the corresponding irradiance values calculated from the surface normals. The experiments show our photometric stereo with auto-radiometric calibration can estimate the surface accurately regardless the nonlinearity of the response function.

3.2 Proposed Method

3.2.1 Lambertian Reflection Model

This section briefly explains the models used to describe the reflection on matte surfaces, the Lambertian reflection model.

The reflectivity of the object depends on its microstructure, orientation, and spatial and spectral distribution, and state of polarization of the incident illumination [28]. For the materials such as chalk or stone, their surface in micro level is, in fact, rough so that the reflected lights scatter in many directions. This is called *diffuse reflection*. If roughness of the surface is uniformly distributed so reflected lights scatter in every direction equally, brightness at a certain point remains same regardless the observer's angle of view. We call this surface has *Lambertian re-*

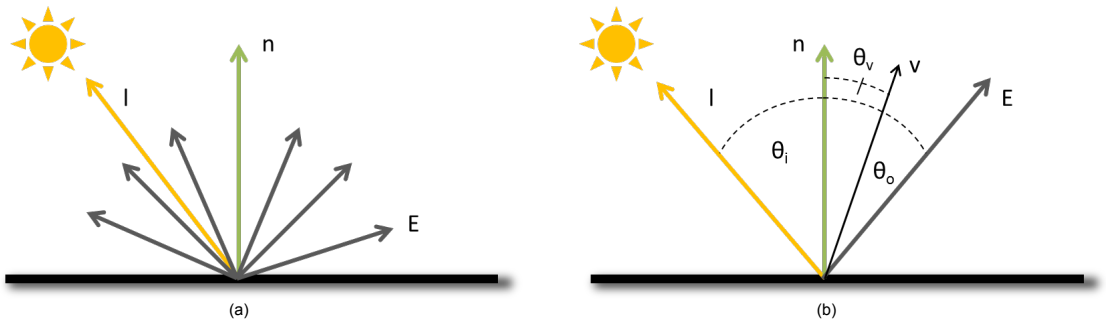

Figure 3.1: (a) Lambertian reflection. The light reflected equally in all direction regardless the viewing direction. Normally, diffuse reflection is modeled as Lambertian reflection. (b) Specular reflection. The incoming light reflects in a particular direction.

flectance property (figure 3.1(a)). The intensity of the reflected light E is,

$$E_{pd} = (\alpha_p \boldsymbol{n}_p)^\intercal \cdot (s_d \boldsymbol{l}_d). \tag{3.1}$$

where α_p is the reflection coefficient or albedo at point p, $\boldsymbol{n}_p$ is surface normal of that point, s_d is the intensity and $\boldsymbol{l}_d$ is a vector represents the direction of incoming light d[1] .

However, bright spots seen on a shiny surface are described by another reflection models. In such surfaces, light reflects off the surface in a particular direction depends on the surface normals and the incoming light direction. This kind of reflection is called *specular reflection*. Though it is possible to find the objects with only diffuse reflection or only specular reflection, most of objects consist of both diffuse reflection and specular reflection.

3.2.2 Photometric Stereo

This section briefly explains the photometric stereo. The classic photometric stereo is a technique to recover the object's geometry and reflectance properties from multiple images under varying known distant light sources [28]. The reflectance characteristics of a surface can be expressed as a reflectance function ϕ of three parameters: surface normal $\boldsymbol{n}_p$, light source direction $\boldsymbol{l}_d$ and viewer's direction $\boldsymbol{v}$. The image intensity E_{pd} can be expressed in reflectance function form as

$$E_{pd} = s_d \phi(\boldsymbol{n}_p, \boldsymbol{l}_d, \boldsymbol{v}). \tag{3.2}$$

Here, s_d denotes the light intensity of light source d. Assuming camera fixed at point $[0, 0, z]$ has orthographic projection, the viewing direction becomes constant

[1]The lighting direction vectors point from the surface of the object to the light source.

along the scene. If we know the direction and intensity of at least three light sources that do not lie on the same plane, we can estimate the surface normals by using linear least square method.

Let $\boldsymbol{N} = [\boldsymbol{n}_1, \ldots, \boldsymbol{n}_p, \ldots, \boldsymbol{n}_P]$ and $\boldsymbol{L} = [\boldsymbol{l}_1, \ldots, \boldsymbol{l}_d, \ldots, \boldsymbol{l}_D]$. If the target object has Lambertian reflectance property, the reflected light E_{pd} depends on only its orientation $\boldsymbol{n}_p$, α_p is the albedo at the point p, the direction of the light is $\boldsymbol{l}_d$ with intensity s_d. With known light directions, and light sources are not on the same plane, the inverse light source matrix $\boldsymbol{L}^{-1}$ is exist. Surface normals and its albedo can be recovered as

$$\alpha_p = \frac{\left\| E_{pd} \cdot \boldsymbol{L}_d^{-1} \right\|}{s_d}, \tag{3.3}$$

$$\hat{\boldsymbol{n}}_p = \frac{1}{\alpha_p} E_{pd} \cdot \boldsymbol{L}_d^{-1}. \tag{3.4}$$

This is equivalent to

$$\hat{\boldsymbol{n}}_p = \arg\min_{\boldsymbol{n}_p} \sum_{l=1}^{L} \left(E_{pd} - \boldsymbol{n}_p^T \boldsymbol{l}_d \right)^2. \tag{3.5}$$

3.2.3 Radiometric Response Function

Typically, image irradiance falling onto an imaging sensor inside a camera is processed through many steps such as white balance, noise reduction, and gamut mapping, etc. We can think of these steps as a function, called *radiometric response function* that maps an irradiance value E into a pixel value I.

Since the radiometric response function is a monotonically increasing function, there is a unique inverse function $g = f^{-1}$ which maps a pixel value I to an irradiance value E.

Hereafter, we normalize the ranges of pixel values and irradiance values to $[0, 1]$ without loss of generality.

In a similar manner to the existing technique [20], we represent the inverse radiometric response function by using polynomials:

$$E = g(I) = \sum_{k=0}^{K} c_k I^k, \tag{3.6}$$

where c_k is the coefficient of the k-th polynomial.

Since the inverse radiometric response function g is also a monotonically increasing function with respect to a pixel value I, the coefficients $\{c_k\}$ satisfy the

monotonicity constraint:

$$\frac{dg(I)}{dI} = \sum_{k=1}^{K} k c_k I^{k-1} > 0, \tag{3.7}$$

when $I > 0$. In addition, since the ranges of pixel values and irradiance values are normalized, the coefficients $\{c_k\}$ satisfy the boundary conditions:

$$g(0) = c_0 = 0, \quad g(1) = \sum_{k=0}^{K} c_k = 1. \tag{3.8}$$

3.2.4 The Simultaneous Estimation

Our proposed method estimates both the surface normals $\boldsymbol{n}_p$ $(p = 1, 2, ..., P)$ and the coefficients of the inverse radiometric response function c_k $(k = 1, 2, ..., K)$ at the same time.

We assume the response function can be approximated with k-order polynomials as shown in eq.(3.6). Substituting the boundary condition (eq.(3.8)) into eq.(3.6) and eliminating c_1, an irradiance E is described by using a pixel value I as

$$\begin{aligned} E &= c_1 I + \sum_{k=2}^{K} c_k I^k \\ &= I + \sum_{k=2}^{K} c_k \left(I^k - I \right). \end{aligned} \tag{3.9}$$

Therefore, in a similar manner to eq.(3.5), the estimates of the surface normals $\{\hat{\boldsymbol{n}}_p\}$ and the coefficients of the inverse radiometric response function $\{\hat{c}_k\}$ are given by

$$\begin{aligned} &(\{\hat{\boldsymbol{n}}_p\}, \{\hat{c}_k\}) = \arg \min_{(\{\boldsymbol{n}_p\}, \{c_k\})} \\ &\sum_{p=1}^{P} \sum_{d=1}^{D} \left[E_{pd} - \boldsymbol{n}_p^T \boldsymbol{E}_d + \sum_{k=2}^{K} c_k \left(E_{pd}^k - I_{pd} \right) \right]^2, \end{aligned} \tag{3.10}$$

Here, the third term in the bracket acts as a correction term for compensating a nonlinear radiometric response function.

As to the monotonicity constraint, substituting eq.(3.8) into eq.(3.7), we obtain

$$\sum_{k=2}^{K} c_k (1 - k I^{k-1}) < 1. \tag{3.11}$$

Therefore, the coefficients have to satisfy this inequality for arbitrary pixel values, *e.g.* $I = i/255$ $(i = 1, 2, ..., 254)$ for 8 bit images.

Thus, the simultaneous estimation of the surface normals and the inverse radiometric response function results in the linear least-square problem in eq.(3.10) with the linear constraints in eq.(3.11). Since this problem is a convex quadratic programming, we can find the globally optimal solution if the number of observations (DP) is larger than the number of unknowns $(3P + K)$. Suppose that the number of pixels P is larger than the number of polynomials K, we can estimate the surface normals and the inverse radiometric response function from four images at least $(D \geq 3 + K/P)$.

When the radiometric response function is linear, we can estimate a surface normal at each surface point independently as shown in eq.(3.5). On the other hand, when it is nonlinear, we cannot deal with each surface point independently as shown in eq.(3.10). Therefore, the naive optimization of eq.(3.10) subject to the constraints of eq.(3.11) is computationally expensive when the number of pixels increases. To reduce the computational cost, we can estimate the inverse radiometric response function (and the surface normals) by using a small number of randomly sampled pixels, and then convert pixel values to irradiance values, and finally estimate the surface normals by using eq.(3.5). Although we did not mention for the sake of simplicity, we detect outliers, *i.e.* shadowed or saturated pixels by using thresholds and remove them from the summations in eq.(3.5) and eq.(3.10).

3.3 Experiments

We used MATLAB implementation of the trust region reflective quadratic programming for optimization. The whole process took about 2.5 seconds for synthetic images and about 7.5 seconds for real images on average by using an Intel Core i7-2600 3.4GHz CPU.

3.3.1 Synthetic Images

We compared the performance of our proposed method with that of the classic photometric stereo [28] by using synthetic images. The target objects are a sphere with uniform albedo and a face with relatively complex shape and non-uniform albedo shown in figure 3.2. The number of images is 16, and the numbers of foreground pixels of the sphere and face are 3228 and 2776 respectively. We used two radiometric response functions: one is the Agfapan APX 400CD and the other is the polynomial $f = E^{0.4}$. We empirically set the number of polynomials in eq.(3.6) as $K = 6$.

In figure 3.3, we show the qualitative results for the sphere. We show the

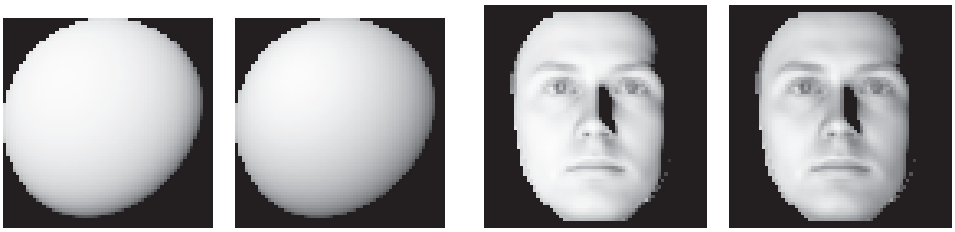

Figure 3.2: Synthetic images of sphere and face with different radiometric response functions.

Table 3.1: Average errors of estimated surface normals and RMS errors of estimated inverse radiometric response functions: synthetic images.

	Surface normal (classic)	Surface normal (ours)	Inverse response function
Sphere(Agfapan)	23.6°	1.6°	0.0056
Sphere(polynomial)	18.7°	1.9°	0.0004
Face(Agfapan)	17.8°	1.7°	0.0068
Face(polynomial)	15.1°	1.7°	0.0004

color coded surface normals[2]: (a) the ground truth, (b) the estimated ones by using the classic photometric stereo, (c) the estimated ones by using our proposed method, and (f) the inverse radiometric response functions: the solid line stands for the ground truth and the dashed line stands for the estimated one. One can see that the estimated surface normals by using our method looks similar to the ground truth while the estimated surface normals by using the classic photometric stereo are significantly distorted. Moreover, one can see that the estimated inverse radiometric response function is almost the same as the ground truth. We show the results for images with the other radiometric response function in (d), (e), and (g). One can see that those results are consistent with (b), (c), and (f).

In figure 3.4, we show the qualitative results for the face. Similar to the experimental results for the sphere, one can see that the estimated surface normals by using our proposed method, *i.e.* (c) and (e) are clearly better than the estimated surface normals by using the classic photometric stereo, *i.e.* (b) and (d). In addition, one can see that the estimated inverse radiometric response functions are almost the same as the ground truths.

Table 3.1 shows the quantitative results: the mean angular errors of the esti-

[2] x, y, and z components ($\in [-1, 1]$) are linearly mapped to RGB.

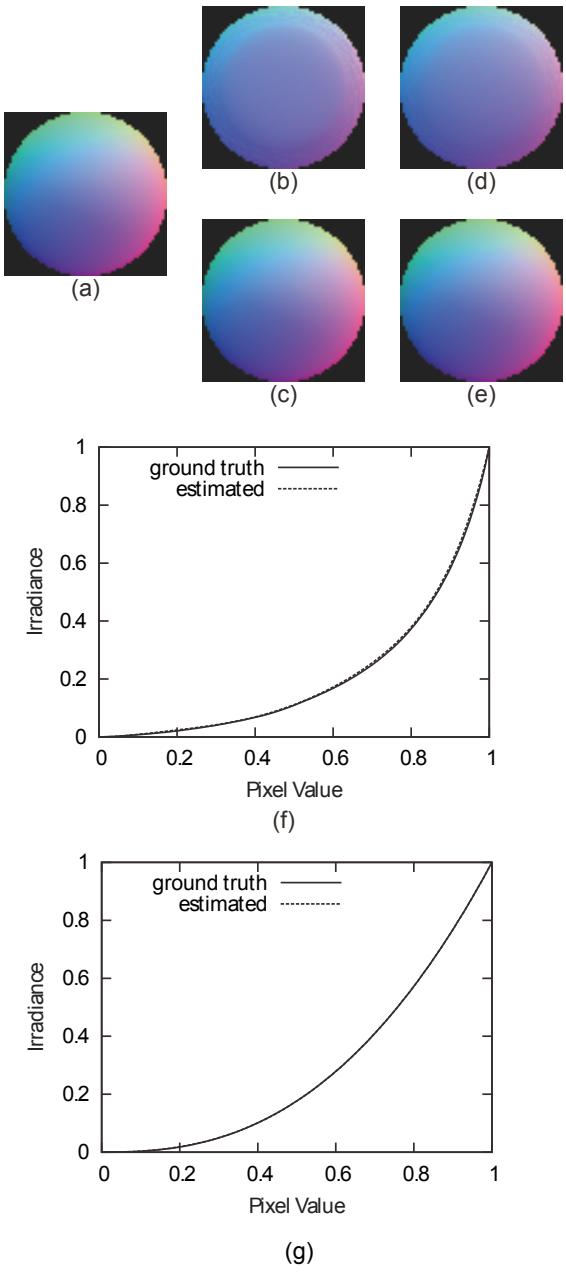

Figure 3.3: Results using synthetic images: sphere. (a) the ground truth, (b) the estimated surface normals by using the classic photometric stereo, (c) the estimated ones by using our proposed method, and (f) the inverse radiometric response functions: the solid line stands for the ground truth and the dashed line stands for the estimated one. (d), (e), and (g) are the results for images with the other radiometric response function.

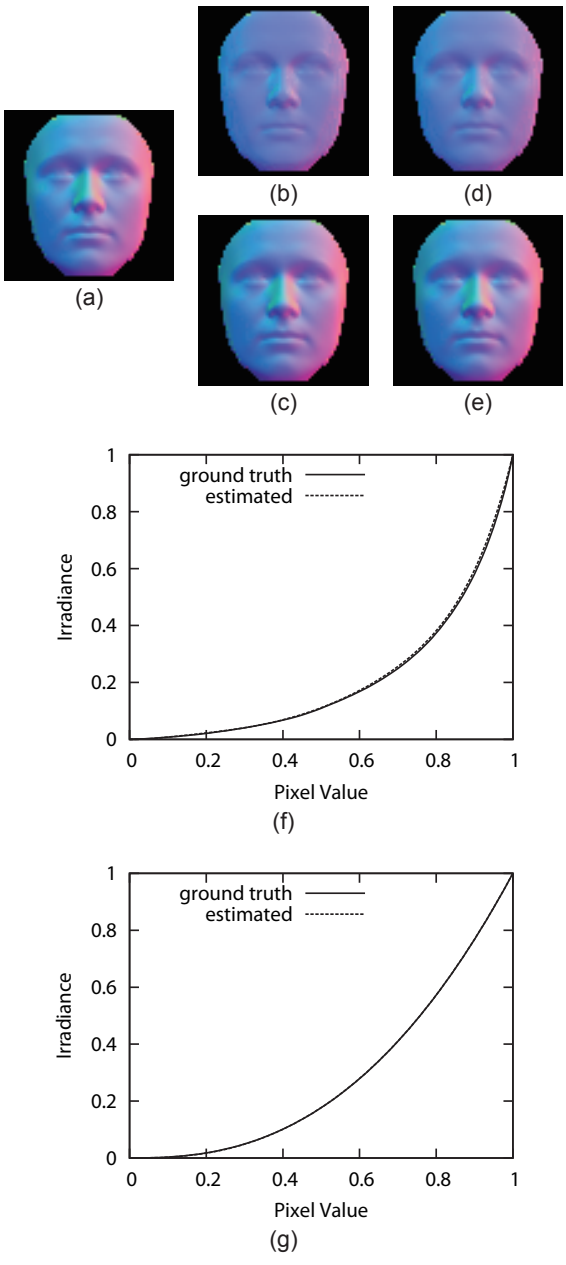

Figure 3.4: Results using synthetic images: face.

mated surface normals and the RMS errors of the estimated inverse radiometric response functions. One can see that the average angular errors of the estimated surface normals are drastically decreased by simultaneously estimating surface normals and a radiometric response function. Moreover, one can see that our proposed method can accurately estimate the inverse radiometric response functions as a by-product.

3.3.2 Real Images

We compared the performance of our proposed method with that of the classic photometric stereo by using real images. The target objects are a sphere and a statue shown in figure 3.5. We captured 10 images by using a Point Grey Chameleon camera with different gamma settings: $g(I) = I^{2.0}$ and $g(I) = I^{0.5}$. The numbers of foreground pixels of the sphere and statue are 7063 and 23115 respectively. We computed the ground truth for the surface normals of the sphere on the basis of its silhouette image. As to the statue, we considered the surface normals estimated by using the classic photometric stereo from images with a linear response function as the ground truth.

In figure 3.6 and figure 3.7, we show the qualitative results for the sphere and the statue. Similar to the experimental results using synthetic images, one can see that the estimated surface normals by using our proposed method, *i.e.*, (c) and (e) are better than the estimated surface normals by using the classic photometric stereo, *i.e.*, (b) and (d). In addition, one can see that the estimated inverse radiometric response function (the dashed line) is close to the ground truth (the solid line). Here, we plot the estimated radiometric response function within the range which covers observed pixel values. The estimated radiometric response function is not necessarily accurate out of the range because there is no observation.

Table 3.2 shows the quantitative results: the average errors of the estimated surface normals and the RMS errors of the estimated inverse radiometric response functions. Similar to the experimental results using synthetic images, one can see that the mean errors of the estimated surface normals are decreased by simultaneously estimating surface normals and a radiometric response function. Moreover, one can see that our proposed method can accurately estimate the inverse radiometric response functions.

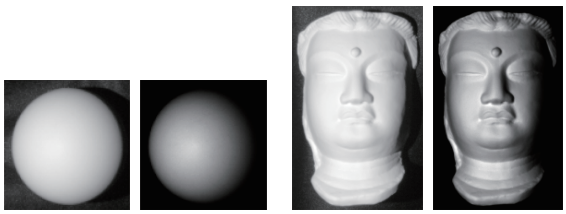

Figure 3.5: Real images of sphere and statue with different radiometric response functions.

Table 3.2: Average errors of estimated surface normals and RMS errors of estimated inverse radiometric response functions: real images.

	Surface normal (classic)	Surface normal (ours)	Inverse response function
Sphere(2.0)	11.3°	2.3°	0.027
Sphere(0.5)	13.1°	3.1°	0.015
Statue(2.0)	11.6°	2.1°	0,021
Statue(0.5)	13.0°	2.6°	0.015

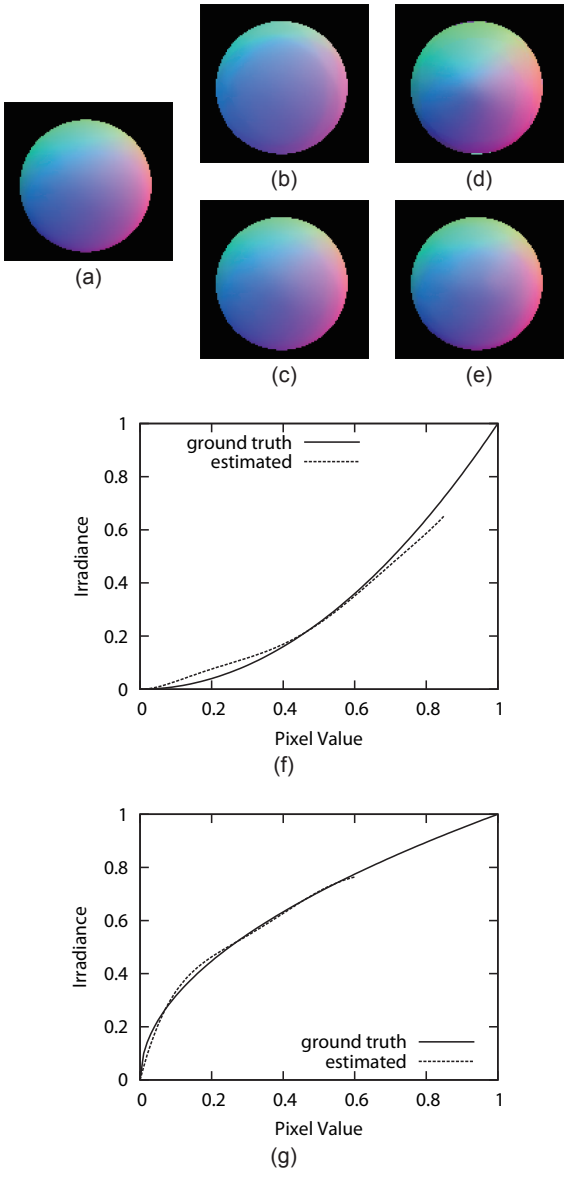

Figure 3.6: Results using real images: sphere.

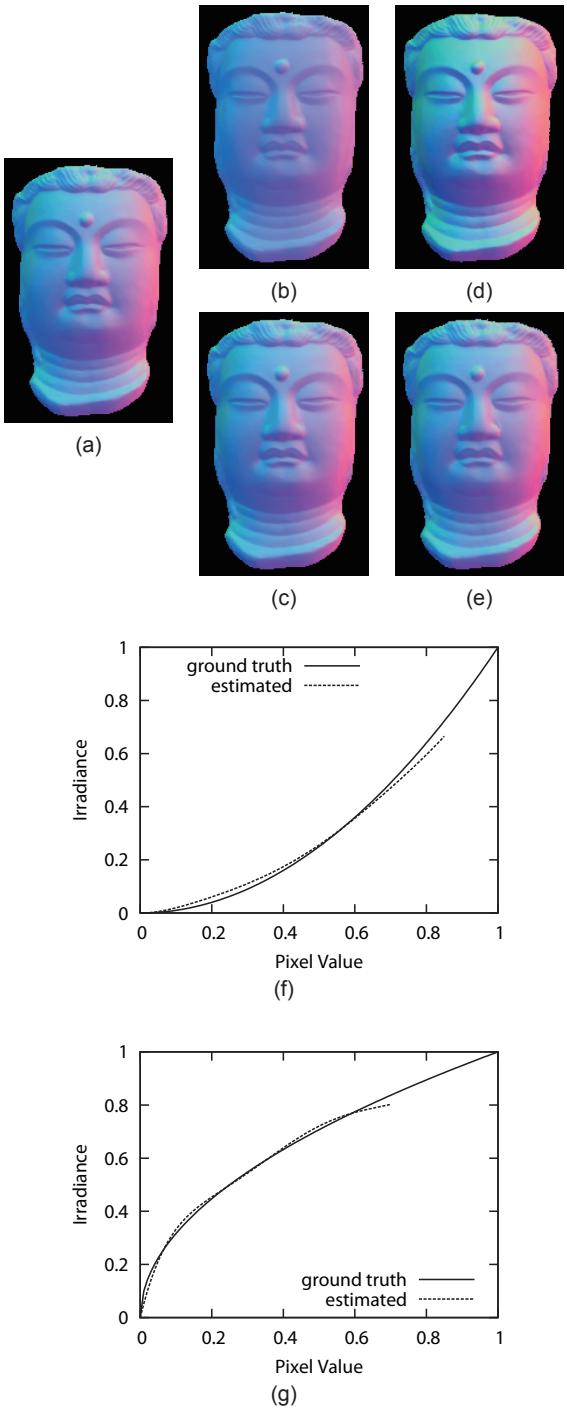

Figure 3.7: Results using real images: statue.

Chapter 4

Extension for Non-Lambertian Materials

Our photometric stereo with auto-radiometric calibration assumes an object with an ideal Lambertian surface, and as a result, the estimated shape and response function are distorted by specular highlights observed in non-Lambertian surfaces. In this chapter, we introduce the extension for non-Lambertian surface to estimate the surfaces of such materials.

4.1 Background

Generally, specular highlights can be easily detected and removed using various techniques such as four-light sources [14, 2], RANSAC [22], or low-rank minimization [29]. However, these methods assume input images are captured by a camera with a linear response function, which is not always true in our case. Therefore, we cannot use these techniques to remove specular highlights in straightforward manner due to nonlinearity of a response function.

Many non-Lambertian surfaces appear as a Lambertian surface except a small area where specular highlights exist, we can treat highlight pixels as outliers which deviate from the Lambert model. Therefore, it would be possible to simultaneously estimate the shape of a non-Lambertian surface and the response function of a camera by incorporating a robust estimation technique such as RANSAC [7] into the auto-radiometric calibration technique.

We conducted a number of experiments on both synthetic and real objects to demonstrate that our proposed method can accurately estimate the surface of given objects with non-Lambertian surface regardless the nonlinearity of response function.

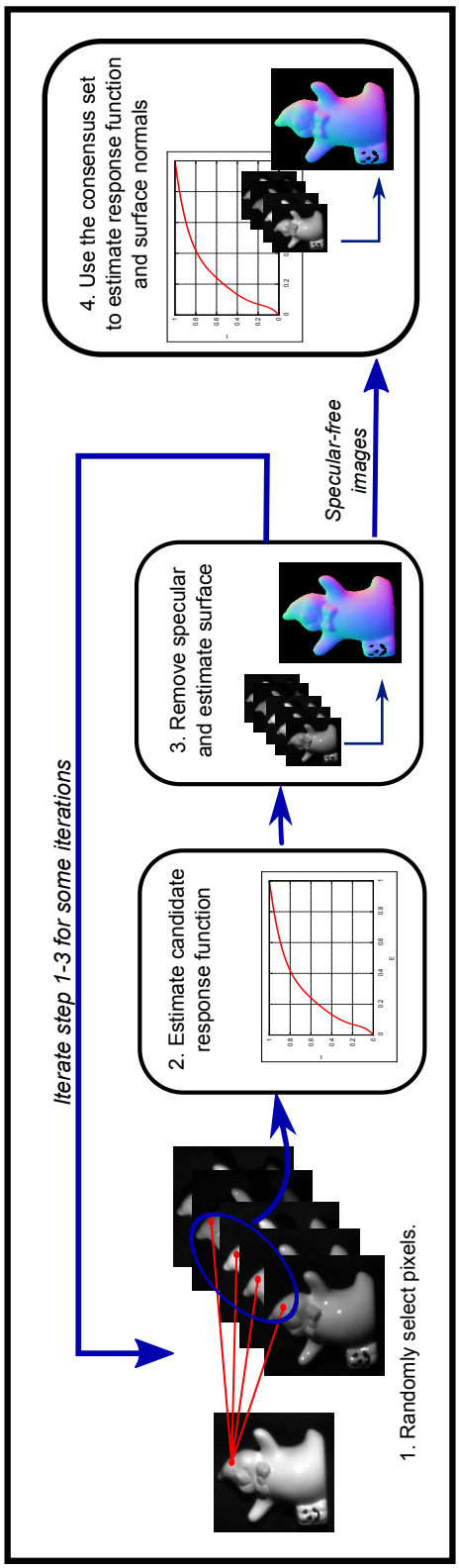

Figure 4.1: Overview of the extension for non-Lambertian surfaces; (1) s ramdom pixels are sampled. t pixel intensities from each sampled pixel are used. (2) Inverse response function is estimated and the input images are calibrated using the estimated function. (3) Specular regions are detected and removed. The diffuse pixels are considered inliers to the Lambertian model. (4) The estimated response function and the estimated shape are evaluated. Step 1-4 are repeated for some iterations to obtain the best specular-free images. (5) The specular-free images are used to estimate response function and shape.

4.2 Proposed Method

As the entire image sequence is affected by the same response function, we can estimate the inverse response function from a small subset of pixel intensities if we assume that number of images is greater than number of unknown coefficients. We apply RANSAC-like algorithm to iteratively determine response function and surface normals by maximizing number of supporting inliers of the estimated inverse response function and surface normals.

For each iteration, s random pixels are sampled and t pixel values that are in the same pixel as each sampled pixel are selected. Then, the selected pixel values are used to estimate a candidate inverse response function. Then, we use the estimated inverse response function to convert the input images into their irradiance form.

Here, assuming the response function is accurately estimated, we remove the outliers once again by applying RANSAC. Then, the diffuse pixel intensities are used to estimate surface normals and, consequently, the irradiance values are estimated according to the Lambertian model. If the inverse response function and the diffuse regions are accurately determined, the estimated irradiance values must equal to the observed irradiance values converted by the inverse response function. Then, the goodness of the estimated inverse response function is determined as the number of inliers, *i.e.*, the number of the estimated irradiance values that equal to the observed irradiance values. These processes are repeated again for some iteration, the diffuse areas from the iteration with the most number of inliers are used to reestimate the response function and surface normals.

The detailed algorithms are given as following.

Step 1. Pixels Random Selection

We select a number of pixel values to estimate a candidate inverse response function. Given the whole set of images are affected by the same response function, we can use only a small subset of pixel intensities to estimate the response function. Let K denotes the degree of polynomials. Firstly, s pixels are randomly selected. Then, the number of required pixel intensities t for a selected pixel p is determined. Since there are 3 unknowns for surface normals for each pixel selected, namely n_{px}, n_{py}, and n_{pz}, plus $K-1$ unknowns for the coefficients of inverse response function, therefore t can be determined as,

$$t = \left\lceil \frac{3 \times s + K - 1}{s} \right\rceil . \tag{4.1}$$

For each selected pixel, t pixel intensities from the same pixel along the set of images are randomly selected.

Although we did not mention for the sake of simplicity, shadows and saturated pixel intensities are removed from the estimation by thresholding. The pixels which have number of pixel intensities less than three after the removal are also excluded from the selection.

Step 2. Estimation of a Candidate Inverse Response Function

A candidate inverse response function g is estimated using the selected pixel intensities. If all of the selected pixel intensities do not consist of specular component, we can determine an inverse response function with eq.(3.10) subjects to the constraint eq.(3.7). Then, the input images are mapped by the estimated inverse response function g into the irradiance $\boldsymbol{E}^{\text{observed}}$.

Step 3. Specular Region Detection and Removal

The specular regions are detected and removed in this step. We utilize a simple pixel intensity comparison which is similar to the one in Barsky [2]. Given specular region is observed within some limited light directions, we can regard a specular pixel intensity as an outlier that does not satisfy the Lambertian model. We apply RANSAC here to iteratively determine the largest subset of pixel intensities that with no specular highlights. Then the appropriate surface normals are estimated from the diffuse pixel intensities.

Assume that the set of images is radiometrically calibrated and converted into their corresponding irradiance $\boldsymbol{E}$. For each point p, three irradiance values, E_{pi}, E_{pj}, and E_{pk} where $1 \leq i, j, k \leq D$, are randomly selected. If the selected irradiance values contain only diffuse component, this becomes the classic photometric stereo case. A unique surface normals $\boldsymbol{n_p}$ can be determined by eq.(3.5). Consequently, we can estimate the irradiance $E_{pd}^{\text{estimated}}$ from the d-th light source $\boldsymbol{l}_d$ and the estimated surface normals $\boldsymbol{n_p}$; the estimated irradiance must be equals to its corresponding observed irradiance E_{pd}^{observed}. On the other hand, if the selected irradiance values contain a specular component, the estimated surface normals becomes distorted and the $E_{pd}^{\text{estimated}}$ becomes inconsistent to the E_{pd}^{observed}. Therefore we measure the goodness of the estimated surface normals by the number of inliers whose estimated irradiance equals to the observed one. The irradiance E_{pd}^{observed} is considered an inlier if following condition is satisfied,

$$|E_{pd}^{\text{estimated}} - E_{pd}^{\text{observed}}| \leq \tau_s E_{pd}^{\text{observed}}, \tag{4.2}$$

where τ_s is a threshold.

The combinations of three irradiance values, E_{pi}, E_{pj}, and E_{pk}, are selected iteratively to obtain a distribution of surface normals. Then, the surface normals $\boldsymbol{n}_p$ is estimated from the inliers of the iteration with highest number of inliers. The specular detection and surface estimation are performed on every foreground pixel to acquire the surface normals $\boldsymbol{n}$.

Step 4 Evaluation of the Candidate Inverse Response Function

The accuracy of the estimated inverse response function is evaluated. If the inverse response function g and the surface normals $\boldsymbol{n}$ are accurately estimated, the irradiance $\boldsymbol{E}^{\text{observed}}$ which mapped by the inverse response g must consistent with the irradiance calculated from the surface property. Hence, we calculate the irradiance $\boldsymbol{E}^{\text{estimated}}$ with the surface normals $\boldsymbol{n}$. We determine the supporting inliers with the same criterion to the specular detection. The irradiance E_{dp}^{observed} supports the estimated inverse response function if it satisfies eq.(4.2).

The step 1 to step 4 are repeated for many iterations to get a numbers of candidate inverse response functions. The inliers for the inverse response function with the largest number of supports are considered diffuse pixel intensities by consensus.

Step 5 Estimation of the response function and surface shape

In this step, the diffuse pixels are used to estimate the inverse response function and the surface normals. The eq.(3.10) and (3.7) are used once again to reestimate the coefficients of the inverse response function $\hat{\boldsymbol{c}}_k$ and the surface normals $\hat{\boldsymbol{n}}$ from the diffuse pixel intensities.

4.3 Experiments

We verified our proposed method by experiments using both synthetic images and real objects. We used MATLAB implementation of the trust region reflective quadratic programming for the optimization. We decide the number of iterations for surface estimation and response function estimation as suggested for RANSAC algorithm[7],

$$\text{number of iterations} = \left\lceil \frac{\log(1-\rho)}{\log(1-w^n)} \right\rceil, \tag{4.3}$$

where ρ is probability that all selected pixel intensities are inliers at least once, w is probability that a selected pixel intensity is an inlier and n denotes sampling

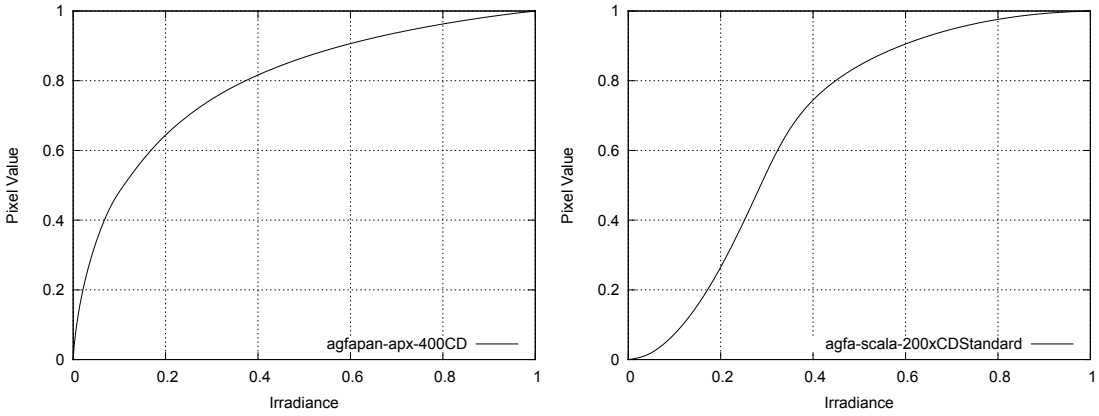

Figure 4.2: Response functions used in the experiments. (left) Agfapan-apx-400CD (right) Agfa-scala-200xCDStandard

size. we set $w = 0.8$ empirically and $n = ts$ for the estimation of response function, we set $w = 3/D$ and $n = 3$ for the specular detection. We set $\rho = 0.99$, $\tau = 0.06$, $s = 1$, and degree of polynomials $K = 6$ are selected empirically for both synthetic images and real objects cases.

4.3.1 Synthetic Images

We evaluate the performance of the extension for non-Lambertian surfaces by comparing the result with that of the classic photometric stereo[28] and result from auto-radiometric calibration photometric stereo for Lambertian surface[21] using synthetic images. The synthetic images were a sphere with uniform albedo and specular factor. We randomly picked ten light directions around the object. We applied two response functions, namely agfa-scala-200xCDStandard1 and agfapan-apx-400CD, from the DoRF database[10] to the rendered images to emulate the effect of nonlinear response function.

Figure 4.4 shows the color coded normal map for the ground truth (a), the estimated ones from the extension for non-Lambertian surfaces (b), the estimated ones from the auto-radiometric calibration photometric stereo without specular detection (d), and the estimated ones from classic photometric stereo (f). Although the estimated surface from the auto-radiometric calibration photometric stereo without specular detection is similar to the ground truth, the distorted areas due to specularity can be easily spotted in the disparity map (e). Figure 4.5 shows the result from the images taken with a different response function.

We plotted the estimated inverse response function in figure 4.6. The plotted function and RMS error were computed using the pixels with intensities less than

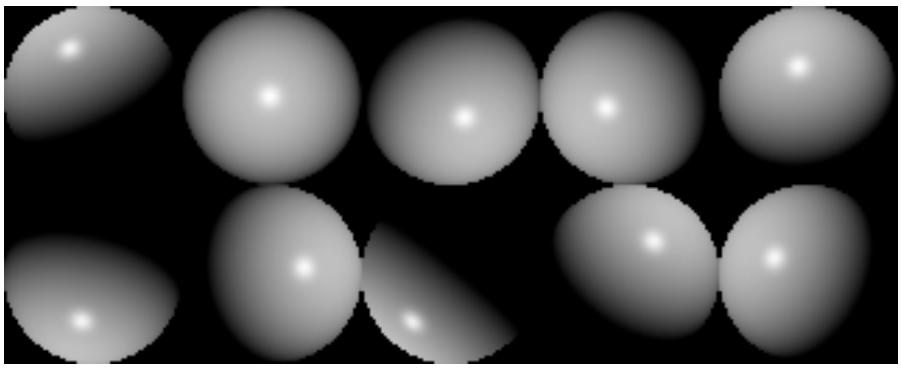

Figure 4.3: Synthetic images: Sphere

Table 4.1: The estimation results for the synthetic sphere. The mean angular errors of the estimated normal maps, and the RMS errors of the estimated response functions.

	Surface normal (classic)	Surface normal (auto-calibrate[21])	Surface normal (the extension)	Inverse response function
Sphere(agfapan)	15.3°	0.6°	**0.2**°	0.001
Sphere(agfascala)	4.24°	0.7°	**0.3**°	0.004

the ninetieth percentile of the largest pixel intensities. This is because the number of bright diffuse pixels is small due to specularity so the estimated function where the pixel intensity is near 1 cannot be constrained well and therefore is not accurate. Moreover, the error propagates to the scale of the estimated response function because we formulate the relationship between an irradiance and a pixel intensity with the boundary conditions $g(0) = 0$ and $g(1) = 1$. Therefore, our algorithm has a kind of ambiguity in the scale of the estimated response function. This ambiguity does not affect the estimated surface normals but it affects the overall scale of the estimated albedos instead.

4.1 shows quantitative results: the mean angular errors of the estimated normals maps compared to the ground truth, and the root mean square error of the scaled estimated functions compared to the ground truth. The errors from the surface estimated by the extension to non-Lambertian surfacess are decreased as there is no distortion due to specularity. The root mean square errors show that our method can accurately estimate the shape of the inverse radiometric response function.

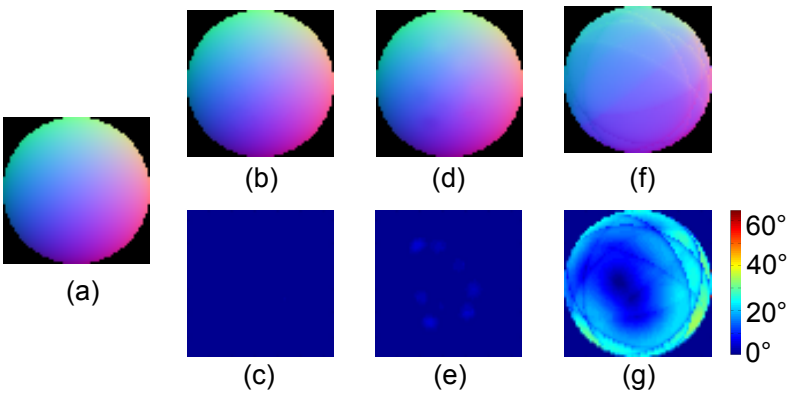

Figure 4.4: The estimated normal map of the synthetic images: sphere (agfapan). (a) ground truth, (b) the normal map estimated from our proposed method and its different to the ground truth, (d) the normal map estimated from the auto-radiometric calibration photometric stereo without specular removal, (f) the normal map estimated by the classic photometric stereo. (c) (e) (g) show the angular differences between the estimated normal maps to the ground truth.

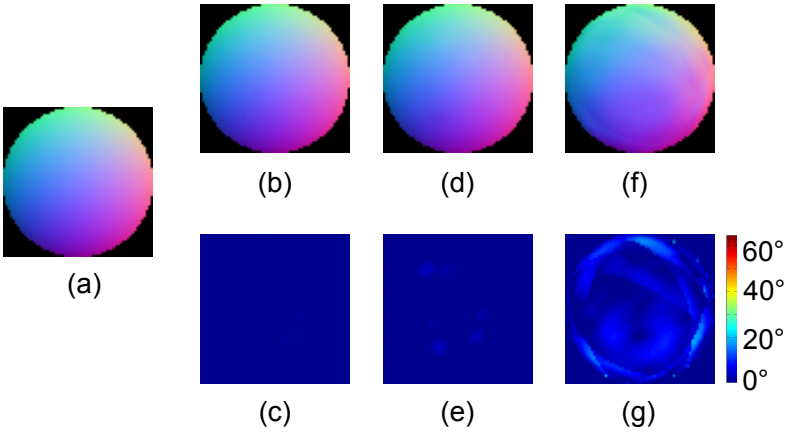

Figure 4.5: The estimated normal maps of the synthetic images: sphere (agfascala).

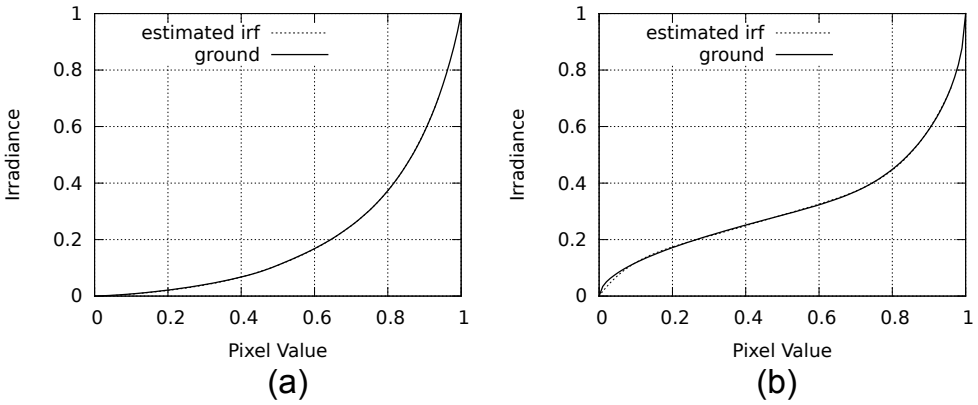

Figure 4.6: The estimated inverse response functions. The graphs were plotted using the first ninetieth percentile of pixel intensities. (a) agfapan-apx-400CD (b) agfa-scala-200xCDStandard.

4.3.2 Real Images

We evaluate the performance of our extension to non-Lambertian surfaces by comparing the result with that of the classic photometric stereo[28] and result from auto-radiometric calibration photometric stereo for Lambertian surface[21] using the images of real objects. The target objects are SEAL, GHOST, TOMATO, and FISH. They are made from ceramics, painted ceramics, shiny plastic, and ceramic with glossy paint respectively. We captured 20 images of each object by using a Point Grey's Flea camera with two nonlinear response functions, namely, agfa-scala-200xCDStandard and agfapan-apx-400CD. We computed the ground truth by using the classic photometric stereo with RANSAC-based specular removal technique on the images captured by the camera with a linear response function.

Same as the synthetic images, we show the RGB color coded normal maps of the surfaces, estimated by our extension to non-Lambertian surfaces, the auto-radiometric calibration photometric stereo with no outliers removal, and the classic photometric stereo method. Our proposed method can remove the specular regions and estimate the surface shape that similar to the ground truth. Moreover, the holes in the bottom part of FISH were estimated correctly (figure 4.14) compared to the result from the classic photometric stereo (f) and the auto-radiometric calibration photometric stereo (d). In addition, our proposed method can estimate the inverse response functions that were similar to the ground truth (fig. 4.16). Similar to the experiments with synthetic images, the estimated functions contained a kind of ambiguity in scale.

Table 4.2 shows quantitative results: the average of the angular error of es-

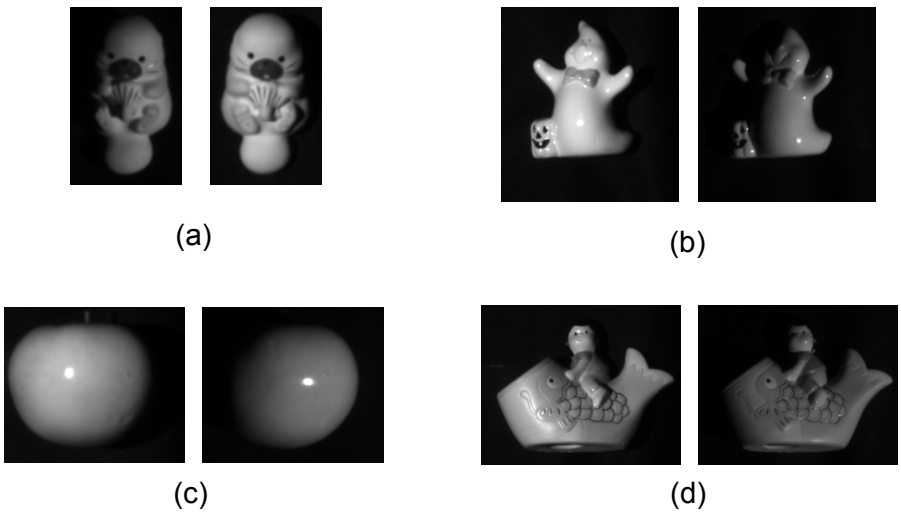

Figure 4.7: Real images: (a) SEAL (b) GHOST (c) TOMATO (d) FISH

timated normals maps compared to the ground truth, and the root mean square error of the scaled estimated functions. Similar to the experiments with synthetic images, the angular errors slightly decreased for our proposed method compared to the auto-radiometric calibration photometric stereo without outlier removal. The root mean square errors show that our proposed method can estimate the shape of the inverse response function accurately even though the observed intensities cover only a part of intensity range.

Table 4.2: The estimation results for the real images sphere when $\tau_s = 0.6$. The average of the angular errors of estimated normal map, and the RMS errors of estimated response function.

	Surface normal (classic)	Surface normal (auto-calibrate [21])	Surface normal (the extension)	Inverse response function
FISH(agfapan)	17.90°	3.89°	**2.22°**	0.0063
FISH(agfascala)	6.91°	3.13°	**2.40°**	0.0055
GHOST(agfapan)	15.35°	3.25°	**1.18°**	0.0409
GHOST(agfascala)	4.27°	1.97°	**1.56°**	0.018
SEAL(agfapan)	14.10°	4.51°	**1.78°**	0.0053
SEAL(agfascala)	6.23°	3.48°	**2.94°**	0.0090
TOMATO(agfapan)	17.90°	2.77°	**1.80°**	0.0075
TOMATO(agfascala)	5.56°	1.76°	**1.69°**	0.0086

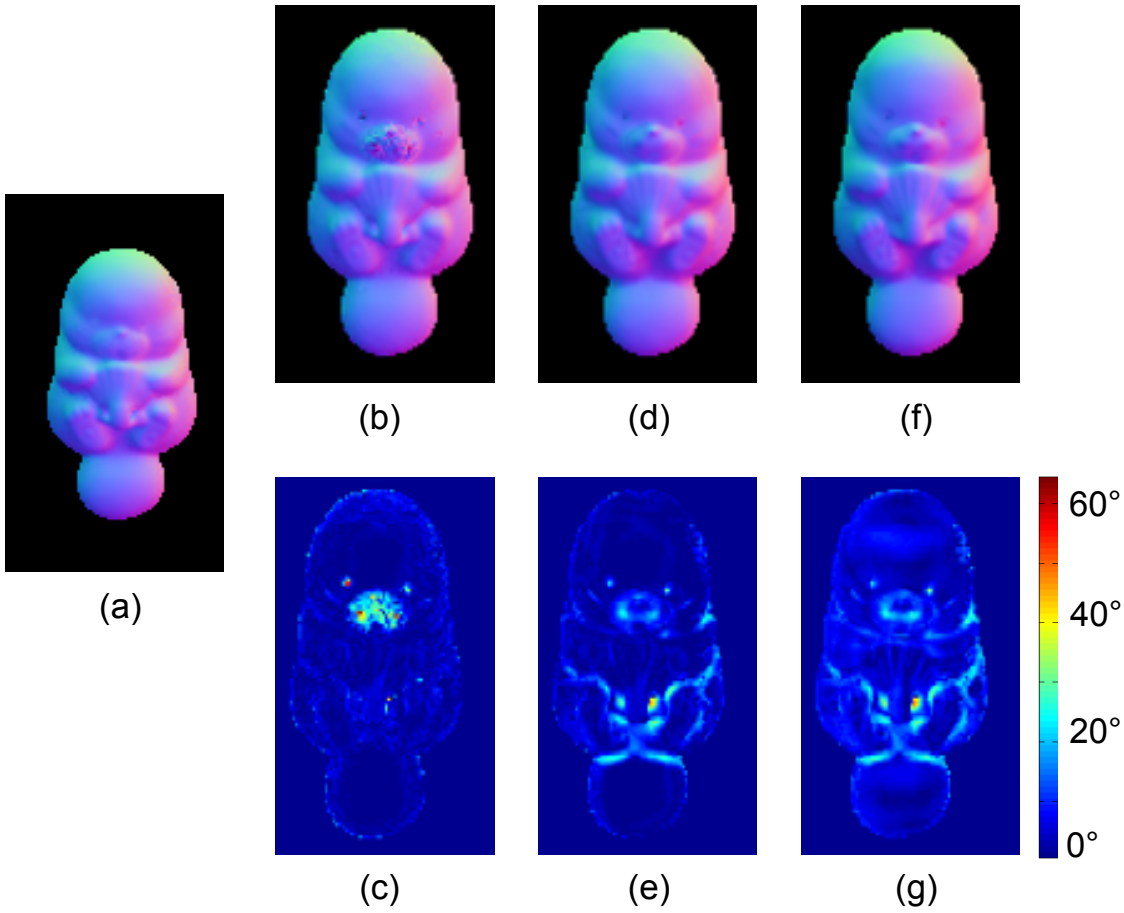

Figure 4.8: The estimated normal maps of the real images: SEAL (agfascala).

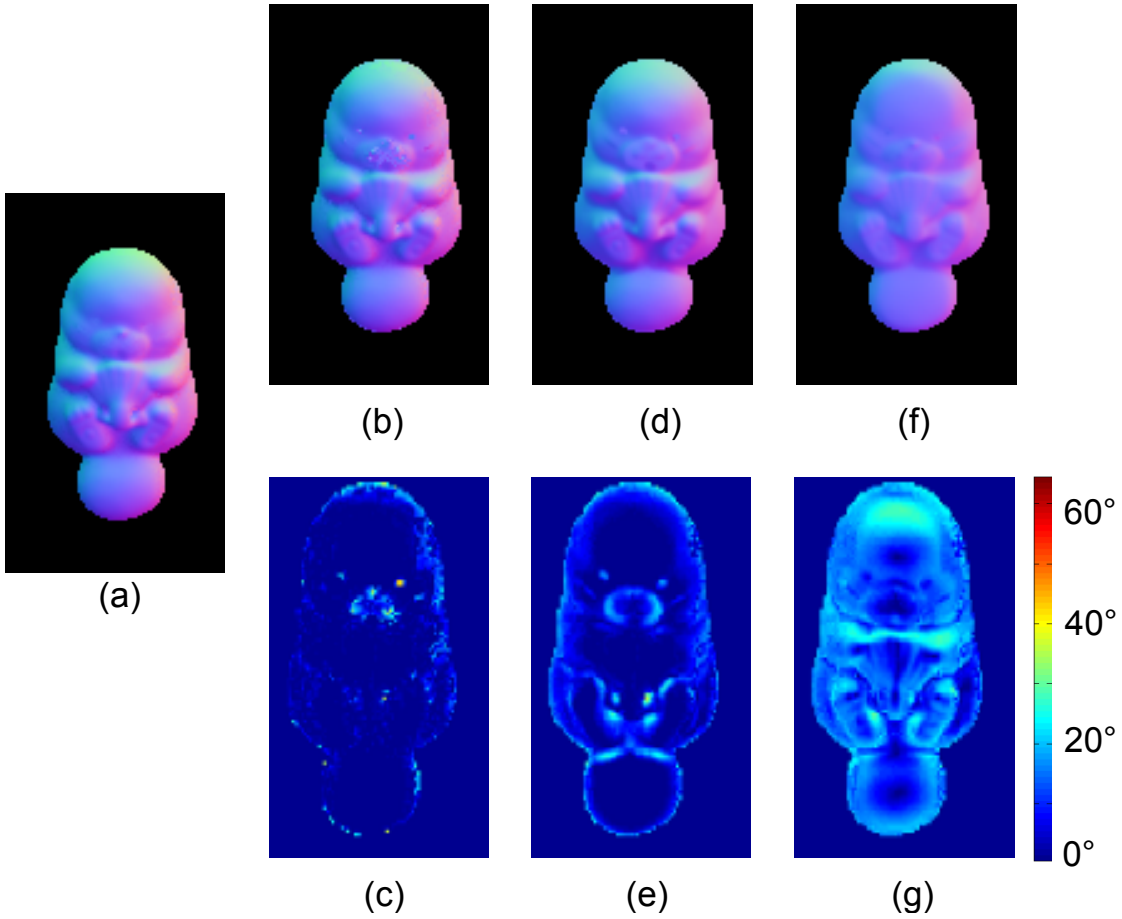

Figure 4.9: The estimated normal maps of the real images: SEAL (agfapan).

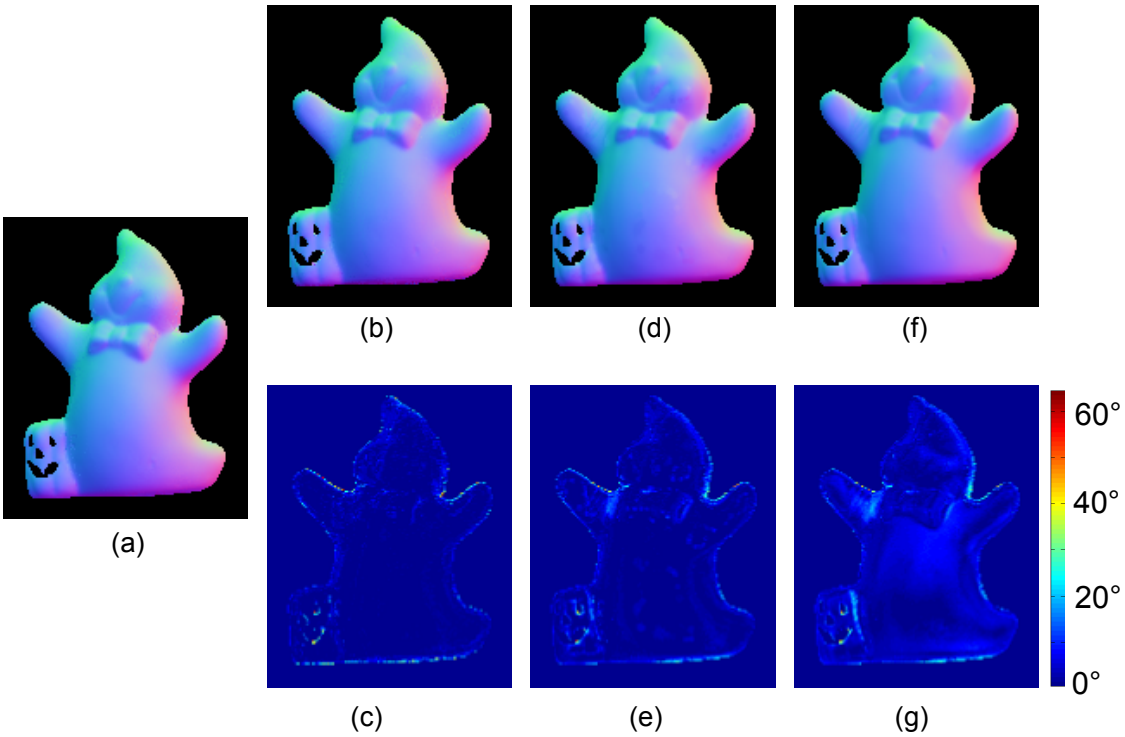

Figure 4.10: The estimated normal maps of the real images: GHOST (agfascala).

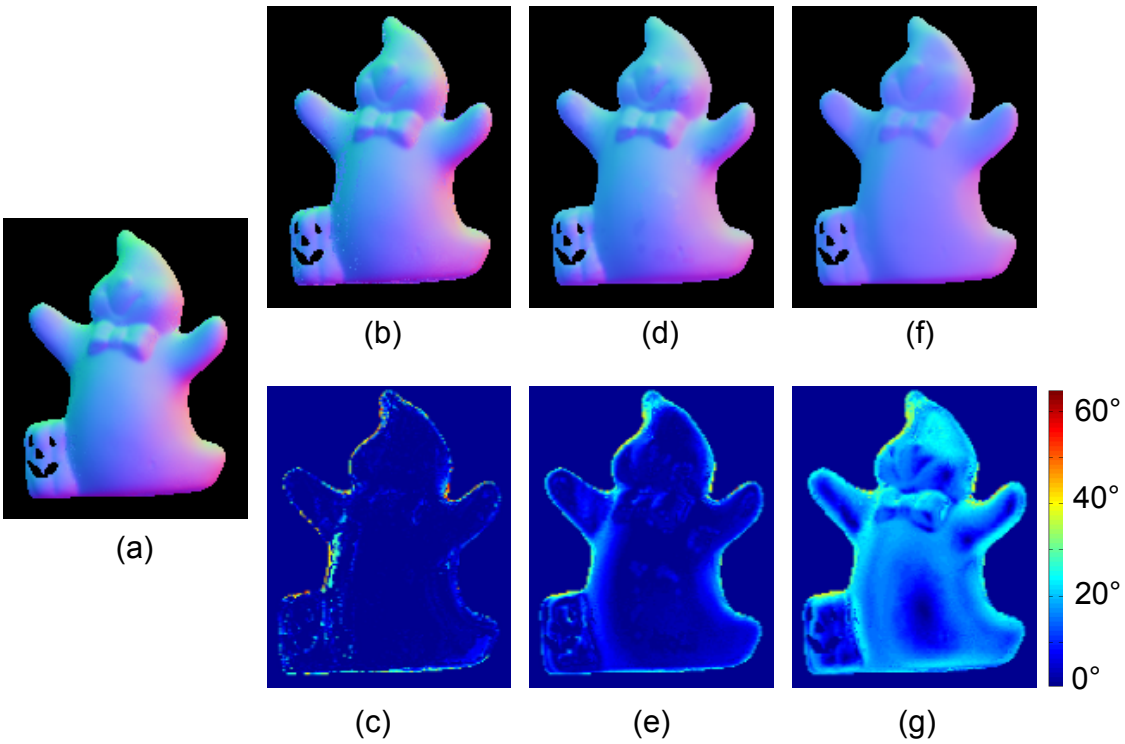

Figure 4.11: The estimated normal maps of the real images: GHOST (agfapan).

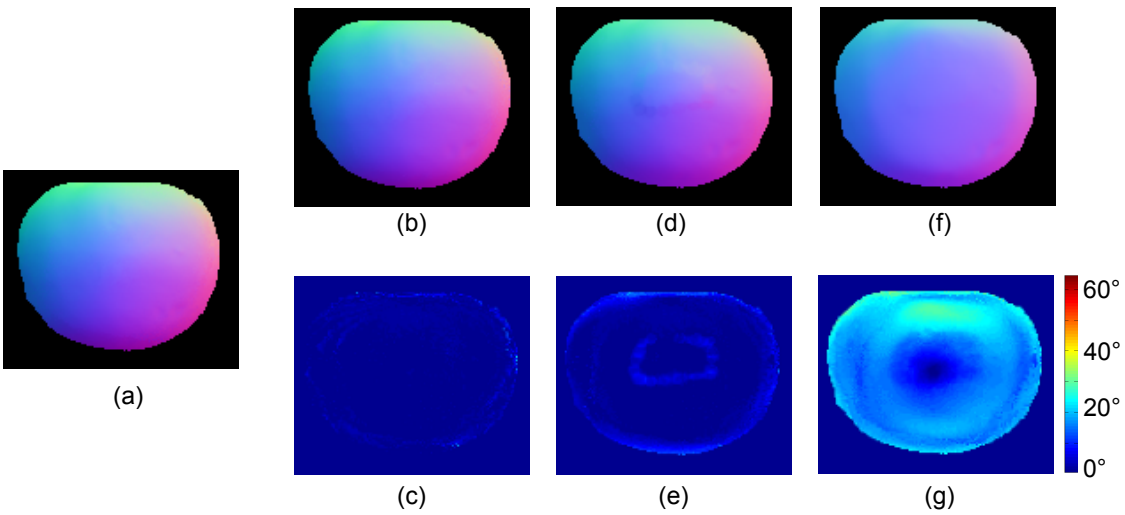

Figure 4.12: The estimated normal maps of the real images: TOMATO (agfapan).

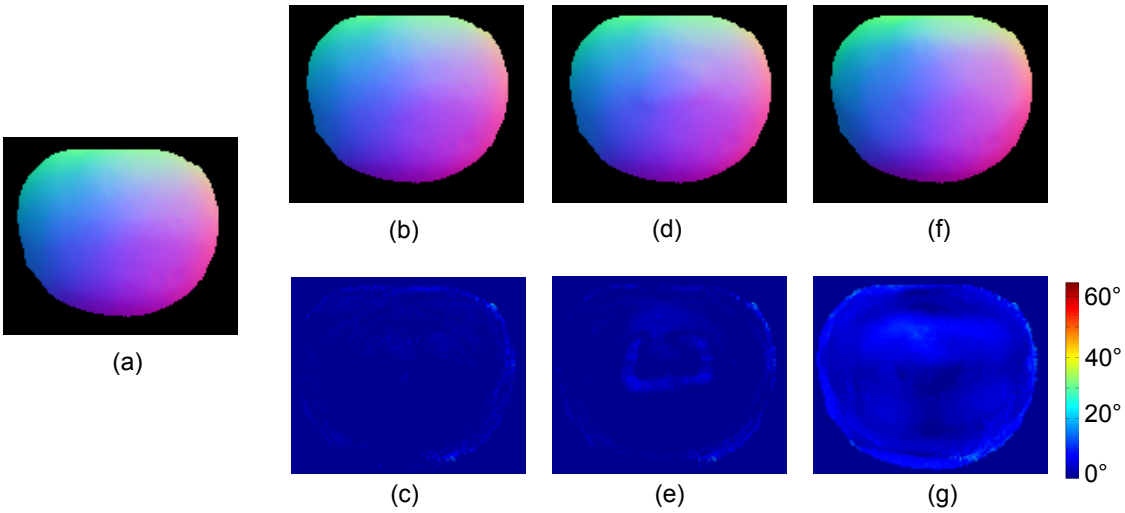

Figure 4.13: The estimated normal maps of the real images: TOMATO (agfascala).

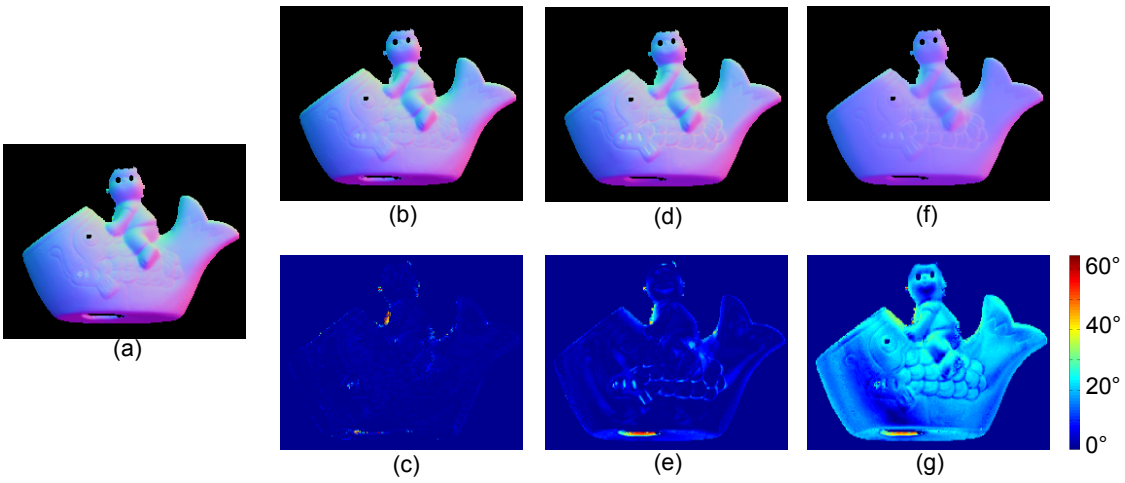

Figure 4.14: The estimated normal maps of the real images: FISH (agfapan).

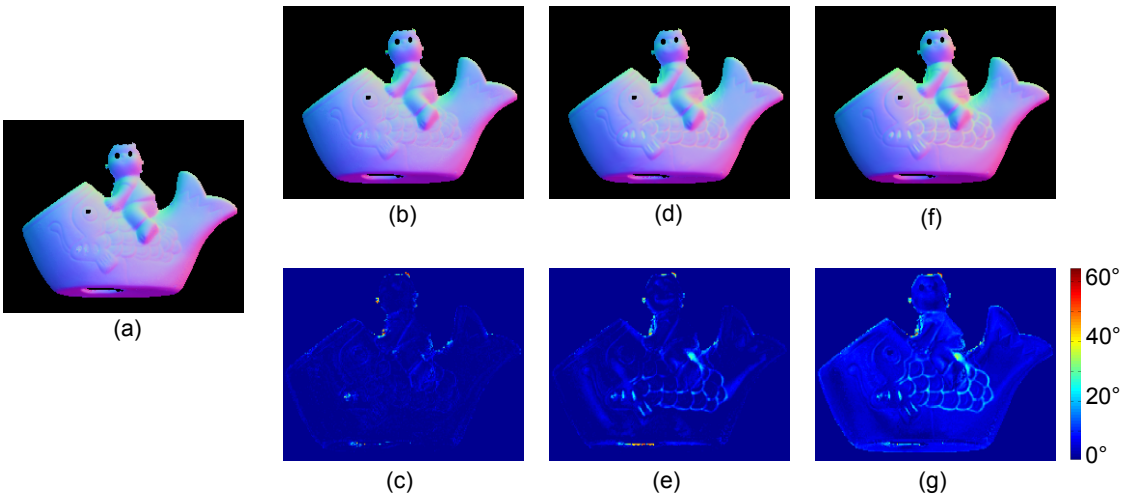

Figure 4.15: The estimated normal maps of the real images: FISH (agfascala).

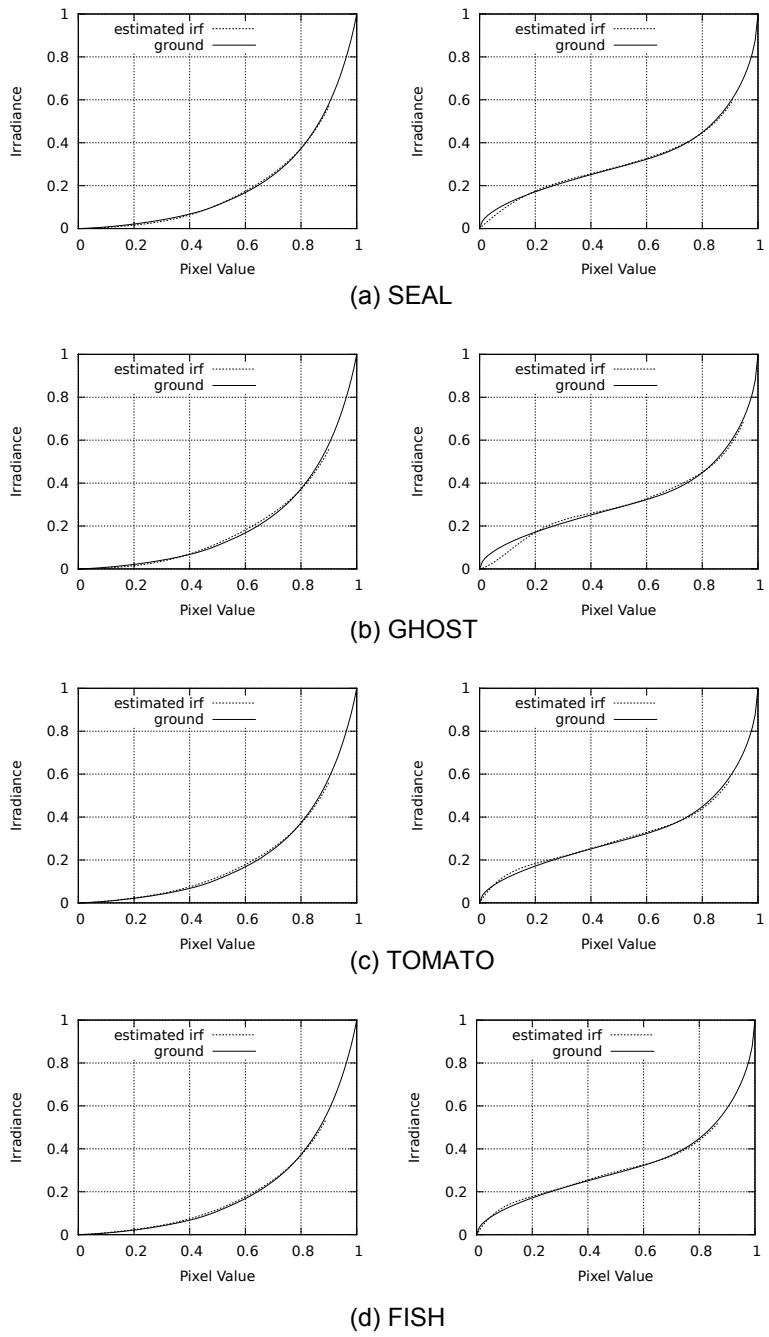

Figure 4.16: The estimated response functions for SEAL, GHOST, TOMATO and FISH.

Chapter 5

Conclusions

This thesis introduces a novel photometric stereo method to recover surface orientations from images captured by a camera with an unknown non-linear response function. The proposed method makes use of the consistency of the irradiance calculated from a reflection model and the irradiance calculated from an inverse response function. Using the proposed method, one can perform photometric stereo with no additional image required for radiometric calibration.

This thesis also proposes the extension for the case of non-Lambertian surfaces with specular hightlights. The extended method treats specular highlights as outliers that deviate from the Lambertian reflection model. The proposed method uses RANSAC-like robust estimations to determine surface normals and a camera response function from pixel intensities that satisfy the Lambertian model.

Future Works

Thus far, the study in this thesis is focused on the case where the directions and the intensities of light sources are known. In order to estimate the surface normals of objects in uncontrolled environments, we need to extend our method for the cases that the directions and the intensities of light sources are unknown, *i.e.*, uncalibrated photometric stereo.

The major problem in uncalibrated photometric stereo is ambiguity of the estimated light sources and the estimated surfaces. Given input images of an object taken from a fixed viewpoint, there are a lot of possible lighting and surfaces combinations that correspond to the input images (figure 5.1). Previous studies made an attempt to solve the ambiguity by using some additional clues, such as distributions of albedos [1], specularities [6, 8], or interreflections [4] that reside in the images. In the future, we hope to integrate such techniques to extend our method for the uncalibrated photometric stereo.

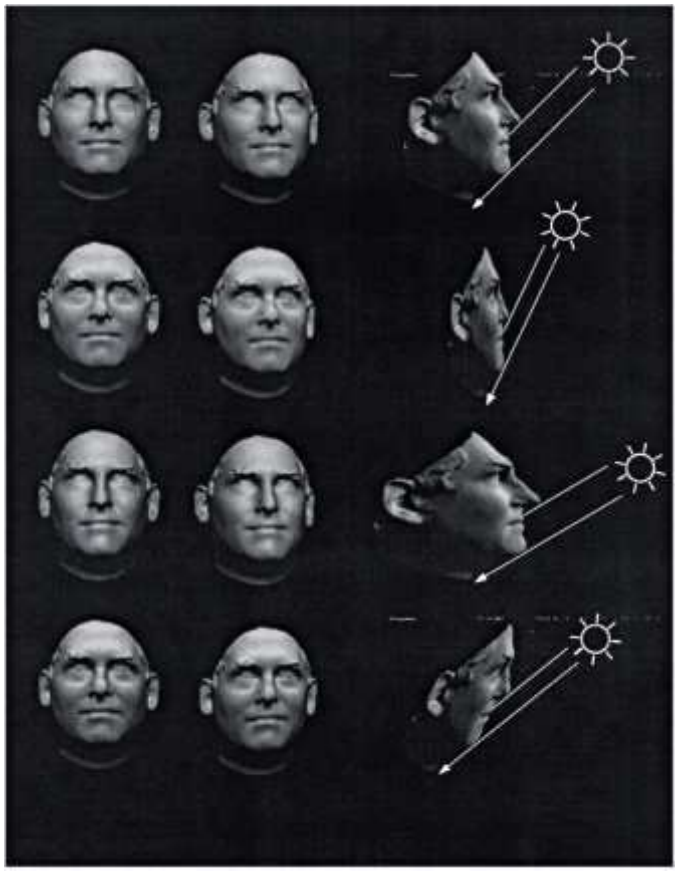

Figure 5.1: This figure illustrates the examples of generalized bas-relief ambiguity. The left two columns are the Lambertian head figures rendered from two different viewpoints. The first row shows the rendered head figures of the true surface and light configuration. The next three rows show the rendered head figures under different GBR transformations. [3]

Bibliography

[1] N. Alldrin, S. Mallick, and D. Kriegman. Resolving the generalized bas-relief ambiguity by entropy minimization. In *Proc. of Computer Vision and Pattern Recognition*, pages 1 –7, Jun. 2007.

[2] S. Barsky and M. Petrou. The 4-source photometric stereo technique for three-dimensional surfaces in the presence of highlights and shadows. *IEEE Trans. Pattern Anal. Mach. Intell.*, 25(10):1239 – 1252, Oct. 2003.

[3] P. Belhumeur, D. Kriegman, and A. Yuille. The bas-relief ambiguity. In *Proc. of Computer Vision and Pattern Recognition*, pages 1060 –1066, Jun. 1997.

[4] M. K. Chandraker, F. Kahl, and D. J. Kriegman. Reflections on the generalized bas-relief ambiguity. In *Proc. of Computer Vision and Pattern Recognition*, pages 788–795, 2005.

[5] P. E. Debevec and J. Malik. Recovering high dynamic range radiance maps from photographs. In *Proc. of Computer Graphics and Interactive Techniques*, pages 369–378, 1997.

[6] O. Drbohlav and R. Sára. Specularities reduce ambiguity of uncalibrated photometric stereo. In *Proc. of European Conference on Computer Vision-Part II*, pages 46–62, May 2002.

[7] M. A. Fischler and R. C. Bolles. Random sample consensus: a paradigm for model fitting with applications to image analysis and automated cartography. *Commun. ACM*, 24(6):381–395, Jun. 1981.

[8] A. Georghiades. Incorporating the torrance and sparrow model of reflectance in uncalibrated photometric stereo. In *Proc. of Int' l Conf. on Computer Vision*, volume 2, pages 816–823, Oct. 2003.

[9] D. Goldman, B. Curless, A. Hertzmann, and S. Seitz. Shape and spatially-varying brdfs from photometric stereo. In *Proc. of Int' l Conf. on Computer Vision*, volume 1, pages 341–348, Oct. 2005.

[10] M. D. Grossberg and S. K. Nayar. Determining the camera response from images: What is knowable? *IEEE Trans. Pattern Anal. Mach. Intell.*, 25(11):1455–1467, Nov. 2003.

[11] T. Higo, D. Miyazaki, and K. Ikeuchi. Multi-view photometric stereo using rough shape data application for estimation of reflection parameters. In *Proc. MIRU 2008*, pages 1280–1287, Jul. 2008.

[12] M. Holroyd, J. Lawrence, G. Humphreys, and T. Zickler. A photometric approach for estimating normals and tangents. *ACM Trans. Graph.*, 27(5):133:1–133:9, Dec. 2008.

[13] S. Ikehata, D. Wipf, Y. Matsushita, and K. Aizawa. Robust photometric stereo using sparse regression. In *Proc. of Computer Vision and Pattern Recognition*, pages 318–325, Jun. 2012.

[14] E. N. C. Jr. and R. Jain. Obtaining 3-dimensional shape of textured and specular surfaces using four-source photometry. *Computer Graphics and Image Processing*, 18(4):309 – 328, 1982.

[15] S. J. Kim and M. Pollefeys. Radiometric alignment of image sequences. In *Proc. of Computer Vision and Pattern Recognition*, volume 1, pages I–645–I–651, 2004.

[16] J.-Y. Lee, B. Shi, Y. Matsushita, I.-S. Kweon, and K. Ikeuchi. Radiometric calibration by transform invariant low-rank structure. In *Proc. of Computer Vision and Pattern Recognition*, pages 2337–2344, Jun 2011.

[17] S. Lin, J. Gu, S. Yamazaki, and H.-Y. Shum. Radiometric calibration from a single image. In *Proc. of Computer Vision and Pattern Recognition*, volume 2, pages II–938–II–945, Jun.-Jul. 2004.

[18] S. Lin and L. Zhang. Determining the radiometric response function from a single grayscale image. In *Proc. of Computer Vision and Pattern Recognition*, volume 2, pages 66–73, Jun. 2005.

[19] S. Mann and R. W. Picard. On being 'undigital' with digital cameras: Extending dynamic range by combining differently exposed pictures. In *Proc. of IS&T*, pages 442–448, 1995.

[20] T. Mitsunaga and S. Nayar. Radiometric self calibration. In *Proc. of Computer Vision and Pattern Recognition*, volume 1, pages 374–380, 1999.

[21] W. Mongkulmann, T. Okabe, and Y. Sato. Photometric stereo with auto-radiometric calibration. In *ICCV Workshops*, pages 753–758, Nov. 2011.

[22] Y. Mukaigawa, Y. Ishii, and T. Shakunaga. Analysis of photometric factors based on photometric linearization. *Journal of the Optical Society of America*, 24(10):3326–3334, Oct. 2007.

[23] S. Nayar, K. Ikeuchi, and T. Kanade. Determining Shape and Reflectance of Hybrid Surfaces by Photometric Sampling. *IEEE Trans. Robot. Autom.*, 6(4):418–431, Aug. 1990.

[24] T. Okabe and Y. Sato. Object recognition based on photometric alignment using ransac. In *Proc. of Computer Vision and Pattern Recognition*, volume 1, pages I–221–I–228, Jun. 2003.

[25] B. Shi, Y. Matsushita, Y. Wei, C. Xu, and P. Tan. Self-calibrating photometric stereo. In *Proc. of Computer Vision and Pattern Recognition*, pages 1118–1125, Jun. 2010.

[26] H. Tagare and R. de Figueiredo. Simultaneous estimation of shape and reflectance maps from photometric stereo. In *Proc. of Int' l Conf. on Computer Vision*, pages 340–343, Dec. 1990.

[27] B. Wilburn, H. Xu, and Y. Matsushita. Radiometric calibration using temporal irradiance mixtures. In *Proc. of Computer Vision and Pattern Recognition*, pages 1–7, Jun. 2008.

[28] R. Woodham. Photometric method for determining surface orientation from multiple images. *Optical Engineering*, 19(1):139–144, 1980.

[29] L. Wu, A. Ganesh, B. Shi, Y. Matsushita, Y. Wang, and Y. Ma. Robust photometric stereo via low-rank matrix completion and recovery. In *Proc. of Asian Conference on Computer vision*, pages 703–717. Springer-Verlag, 2011.

Publications

1. モンコンマーン　ウィーンナート, 岡部　隆弘, 佐藤　洋一, ”カメラ応答関数の自動校正を伴う照度差ステレオ : 非ランバート物体への拡張”. 2013-CVIM-185(3), pp.1-8, Jan. 2013.

2. Wiennat Mongkulmann, Takahiro Okabe, Yoichi Sato, ”Automatic Radiometric Calibration in Photometric Stereo by Using Irradiance Consistency”. 2011-CVIM-179(21), pp.1-7, Nov. 2011.

3. Wiennat Mongkulmann, Takahiro Okabe, and Yoichi Sato, “Photometric stereo with auto-radiometric calibration”, in ICCV Workshops, pp. 753-758, Nov. 2011.